University of Reading

# *Air pollution modulates trends and variability of the global methane budget*

Article

Accepted Version

Zhao, Y., Zheng, B., Saunois, M., Ciais, P., Hegglin, M. I. ORCID: https://orcid.org/0000-0003-2820-9044, Lu, S., Li, Y. and Bousquet, P. (2025) Air pollution modulates trends and variability of the global methane budget. Nature, 642. pp. 369-375. ISSN 0028-0836 doi: 10.1038/s41586-025-09004-z Available at https://centaur.reading.ac.uk/123769/

It is advisable to refer to the publisher's version if you intend to cite from the work. See Guidance on citing.

To link to this article DOI: http://dx.doi.org/10.1038/s41586-025-09004-z

Publisher: Nature Publishing Group

All outputs in CentAUR are protected by Intellectual Property Rights law, including copyright law. Copyright and IPR is retained by the creators or other copyright holders. Terms and conditions for use of this material are defined in the End User Agreement.

www.reading.ac.uk/centaur

**CentAUR**

University of Reading

Central Archive at the University of Reading

Reading's research outputs online

# Air pollution modulates the trends and variations of global methane budget

Yuanhong Zhao[1], Bo Zheng[2]*, Marielle Saunois[3], Philippe Ciais[3], Michaela I. Hegglin[4,5], Shengmin Lu[1], Yifan Li[2], Philippe Bousquet[3]

[1] College of Oceanic and Atmospheric Sciences, Ocean University of China; Qingdao, 266100, China.
[2]Shenzhen Key Laboratory of Ecological Remediation and Carbon Sequestration, Institute of Environment and Ecology, Tsinghua Shenzhen International Graduate School, Tsinghua University; Shenzhen, 518055, China.
[3]Laboratoire des Sciences du Climat et de l'Environnement, LSCE-IPSL (CEA-CNRS-UVSQ), Université Paris-Saclay; Gif-sur-Yvette, 91191, France.
[4]Institute of Climate and Energy Systems, Stratosphere (ICE-4), Forschungszentrum Jülich; Jülich, 52425, Germany.
[5]Department of Meteorology, University of Reading, Reading, RG6 6ET, United Kingdom.

* Correspondence to: Bo Zheng (bozheng@sz.tsinghua.edu.cn)

## Abstract

Reactive air pollutants both produce and consume hydroxyl radical (OH) in the troposphere, playing a pivotal role in regulating the chemical sink of methane ($CH_4$)[1]. However, a comprehensive quantification of this interaction over decadal timescales remains incomplete[2]. Here we developed an integrated observation- and model-driven approach to quantify how variations in key air pollutants influence the $CH_4$ chemical sink and alter the $CH_4$ budget. Our results indicate that from 2005 to 2021, enhanced ozone ($O_3$), increased water vapor, and decreased carbon monoxide (CO) collectively contributed to a growth of the global $CH_4$ sink by 1.3–2.0 Tg $yr^{-2}$, thereby buffering atmospheric $CH_4$ growth rates. This increase was primarily concentrated in tropical regions and exhibited a north-south asymmetry. Periods of abnormal $CH_4$ growth were typically linked to abrupt OH level changes driven by fluctuations in the air pollutants, especially during extreme events like mega wildfires and the COVID-19 pandemic. Our study uncovers a tradeoff between $O_3$ pollution control and $CH_4$ removal mediated by OH and highlights the risk of increasing CO emissions from widespread wildfires.

## Main

Air pollution affects climate through various complex interactions. It perturbs the Earth's radiative energy balance and alters the atmospheric oxidation capacity, which determines the lifetimes of short-lived climate forcers[1]. A pivotal mechanism in this dynamic is the impact on hydroxyl radical (OH), the most important oxidant in the troposphere, which accounts for approximately 90% of the methane ($CH_4$) chemical sink[2]. As the second largest greenhouse gas, the global $CH_4$ levels have risen sharply since 2007[3]. Besides the anthropogenic[4] and wetland emissions[5,6], the reaction with OH is also a key factor that modulates the trend and variations of global $CH_4$ burden[7]. Tropospheric OH has a short lifetime on the order of seconds and is extremely reactive with reactive trace gas air pollutants like carbon monoxide (CO), ozone ($O_3$), nitrogen oxides ($NO_x$=NO+$NO_2$), and non-methane volatile organic compounds (NMVOCs)[8]. Efforts to mitigate air pollutants have intensified worldwide since 1990 for protecting both public health and ecosystems[9]. This raises questions about how air pollution changes have influenced the global $CH_4$ removal by OH in recent decades[2]. Addressing this question requires a comprehensive, detailed quantification of the impacts of various air pollutants on the global burden of OH and the chemical sink of $CH_4$.

Tropospheric OH is primarily produced through the reaction of water vapor ($H_2O_{(g)}$) with excited oxygen atoms ($O^1(D)$) and by the reaction of nitrogen oxide (NO) with hydroperoxyl radical ($HO_2$) and organic peroxy radicals ($RO_2$). The $O^1(D)$ is generated from the photolysis of $O_3$ ($\lambda$ <340 nm) and influenced by the overhead $O_3$. The primary sinks for tropospheric OH include its reactions with CO, $CH_4$, and NMVOCs, and radical-radical reactions, with CO dominating OH removal[10]. Alterations in these chemical reactions control the abundance of tropospheric OH, which can be diagnosed by atmospheric chemistry models[11-15]. However, these models often exhibit discrepancies between simulated and observed pollutant concentrations, indicating underlying shortcomings in the model transport and chemistry mechanisms or uncertainties in the emission databases used[12,13,16]. Satellite observation data of air pollutants are being exploited to investigate OH variations[17], based on OH proxies[18-21], machine learning methods[22-24], and simplified steady-state approach[25]. While these methods are effective for predicting spatiotemporal variations in OH, they have limitations in attributing these variations to specific OH precursors. Comprehensive quantification of the impact of various OH precursors on the global $CH_4$ budget is still in its infancy[2].

Building on the methods of previous studies[26], we developed an integrated observation- and model-driven approach to reconstruct global tropospheric OH variations caused by the main OH precursors, including CO, $O_3$, $CH_4$, $NO_x$ (referring to boundary $NO_x$ if not mentioned specifically), total column $O_3$ ($TCO_3$), and $H_2O_{(g)}$ from 2005 to 2021 (Methods). By integrating state-of-the-art atmospheric composition fields and model tools, we diagnosed the impact of the main OH precursor variations on the global OH levels, providing new insights into their spatiotemporal variations, drivers, and impacts on the $CH_4$ budget.

## Trends and variations of global OH

The derived global tropospheric column-averaged, air-mass-weighted OH concentration ($[OH]_{trop\text{-}M}$) driven by the aforementioned precursors increased significantly by 0.2–0.4% $yr^{-1}$ from 2005 to 2021 (Mann-Kendall test, P<0.05) (Fig. 1a). This trend is robust accounting for uncertainties arising from OH precursor concentrations and chemical mechanisms, estimated using the Monte Carlo method. Based on the two different chemical mechanisms, MOZART and GEOS-Chem (Methods), the global mean $[OH]_{trop\text{-}M}$ was estimated to have increased by $0.5\pm0.09\times10^5$ (mean±standard deviation) molec $cm^{-3}$ and $0.3\pm0.06\times10^5$ molec $cm^{-3}$, respectively, between the two five-year periods, 2005–2009 and 2015–2019. This rise in OH

levels corresponds to increases of 22.8±5.1 Tg $yr^{-1}$ and 14.7±3.6 Tg $yr^{-1}$ in the $CH_4$ sink. $[OH]_{trop\text{-}M}$ exhibited increases during 2007–2009 ($0.4\times10^5$ molec $cm^{-3}$) and 2015–2016 ($0.3\times10^5$ molec $cm^{-3}$), and decreases during 2013–2015 ($-0.2\times10^5$ molec $cm^{-3}$) and 2019–2021 ($-0.2\times10^5$ molec $cm^{-3}$). These fluctuations reflect the large impacts of abrupt changes in atmospheric compositions on OH due to extreme events like El Niño[11,27] and the Coronavirus Disease 2019 (COVID-19) lockdowns[28], which will be discussed further below. During other years, $[OH]_{trop\text{-}M}$ showed variations of less than $0.1\times10^5$ molec $cm^{-3}$.

The net variations in OH driven by these precursors closely mirror the interannual changes in global $CH_4$ atmospheric growth rates (Fig. 1b). Years with negative anomalies in global $[OH]_{trop\text{-}M}$, such as 2007, 2014, 2015, 2020, and 2021, coincide with sudden surges in the growth rates of $CH_4$ mixing ratios compared to adjacent years. In contrast, periods with positive anomalies in global $[OH]_{trop\text{-}M}$ are associated with reduced $CH_4$ growth rates, as observed during 2007–2009 and 2015–2016. Although the atmospheric $CH_4$ burden is controlled by both sources and sinks, the inverse relationship between the annual growth rates of $CH_4$ and net OH variations suggests that the OH precursors considered in this study, such as $O_3$, CO, and $NO_x$, and $H_2O_{(g)}$, play a critical role in governing the $CH_4$ budget, particularly during years with abrupt changes.

Our estimates of $[OH]_{trop\text{-}M}$ show interannual variations of ±2–5% between 2005 and 2021, which broadly align with previous studies that used methyl-chloroform (MCF) inversions in atmospheric models (±3–6%)[29,30] and hydrofluorocarbon species (HFCs) inversions based on box models (±2%)[31] (Extended Data Fig. 1). Despite discrepancies across different inversion results, our precursor-based estimates effectively capture key features of OH interannual variations identified by the MCF inversions, such as the negative anomalies around 2007 and 2015 and the subsequent rebounds[30]. The positive trend in $[OH]_{trop\text{-}M}$ from our precursor-based estimates is not detected by the atmospheric inversions but is consistent with the satellite-based estimate of a positive trend during 2005–2019 (0.21% $yr^{-1}$ over tropical oceans) using a machine learning method[22]. The positive trends of OH since 2005 follow the positive OH trend during 1980–2010 derived from the model ensemble of the Chemistry–Climate Model Initiative[11]. The consistency indicates that the precursors included in our analysis represent the major drivers of tropospheric OH variations, even though limited to specific precursor species with available and reliable observation datasets. Therefore, our precursor-based estimates provide valuable insights into the factors driving changes in the global $CH_4$ chemical sink.

**Impacts on the global $CH_4$ budget**

During 2005–2021, variations in the concentrations of CO, $H_2O_{(g)}$, $NO_x$, and $O_3$ contribute to a global rise in OH levels (Figs. 2a–d). Among these precursors, on the global scale, CO concentration levels have declined, while $H_2O_{(g)}$, $NO_x$, and $O_3$ have increased. The steady decline in global CO concentrations since 2005 is primarily attributed to improved fossil fuel combustion efficiency, which has substantially reduced anthropogenic CO emissions[32]. This decline has offset the rising CO chemical production from $CH_4$ and NMVOC oxidations as well as the stabilizing CO emissions from wildfires[33]. The increase in tropospheric $NO_x$ and $O_3$ is likely due to the growth in anthropogenic emissions (e.g., $NO_x$, VOCs) over the past two decades, particularly in emerging countries[34]. The rise in $H_2O_{(g)}$ levels is caused by global warming[35]. Not all human-caused changes in atmospheric composition led to rising OH. The increasing $TCO_3$, which reduces the $O^1(D)$ photolysis rates, and rising $CH_4$ burdens both drove down OH, although these factors were not sufficient to counterbalance the increasing tendency of OH driven by the other precursors (Figs. 2e and f). Overall, human-induced air pollution, encompassing both improvements (e.g., CO reduction) and deteriorations (e.g., increased $NO_x$ and $O_3$), along with accelerated global warming, have increased global OH levels since 2005.

The atmospheric lifetimes of $NO_x$, CO, $H_2O_{(g)}$, and $O_3$ range from hours to months in the troposphere, leading to spatial-temporal variations in their concentrations that affect the interannual anomalies of OH. For instance, the OH changes induced by CO exhibit large variability because of the variable CO emissions from wildfires (Fig. 2a), which are highly sensitive to extreme fire weather[33]. The vast wildfire CO emissions in 2015, caused by El Niño, led to pronounced negative anomalies in OH. Similarly, a notable decline in $[OH]_{trop\text{-}M}$ of 0.1–$0.2\times10^5$ molec $cm^{-3}$ $yr^{-1}$ was observed in 2020 and 2021 (Fig. 1a), primarily due to reduced $O_3$ levels related to the reduction of $NO_x$ emissions during the COVID-19 pandemic (Fig. 2d).

We further evaluated the impacts of OH precursors on the decadal changes in the global $CH_4$ budget from 2005–2009 to 2015–2019 (Fig. 2g). Our estimates indicate an increase in $CH_4$ sink of 22.8±5.1 Tg $yr^{-1}$ and 14.7±3.6 Tg $yr^{-1}$, derived respectively from the OH fields from the MOZART and GEOS-Chem mechanisms (Fig. 1a). Rising tropospheric $O_3$ accounted for approximately 40% of the increase in the global $CH_4$ sink over these periods, with estimates of 13.1 (min–max range of 9.7–16.5) Tg $yr^{-1}$ for MOZART and 8.6 (6.9–10.3) Tg $yr^{-1}$ for GEOS-Chem. Increasing $H_2O_{(g)}$ was the second most important driver, contributing about 30% to the $CH_4$ sink increase, with estimates of 9.7 (9.5–9.8) Tg $yr^{-1}$ for MOZART and 7.7 (7.4–7.9) Tg $yr^{-1}$ for GEOS-Chem. Decreasing CO resulted in a modest increase in the $CH_4$ chemical sink, estimated at 4.3 (2.2–6.4) Tg $yr^{-1}$ for MOZART and 3.0 (1.5–4.5) Tg $yr^{-1}$ for GEOS-Chem. Despite the differing magnitude estimates based on the two chemical mechanisms, they ranked the impacts of the different precursors on the changes in the $CH_4$ chemical sink in the same order of importance. The increases in the global $CH_4$ sink due to $O_3$, $H_2O_{(g)}$, and CO are comparable to, and in some cases exceed, the growth in $CH_4$ emissions from major anthropogenic (e.g., agriculture and waste) and natural (e.g., fire and wetland) sources during the same period. Our results confirm that the variations in the air pollutants play a crucial role in shaping the global $CH_4$ budget, alongside shifts in $CH_4$ emission sources.

$NO_x$ affects tropospheric OH burden and $CH_4$ budget not only through tropospheric $O_3$ formation but also directly participates in OH production and loss pathways. Compared to the indirect effects via $O_3$, the direct impacts of $NO_x$ concentrations in the boundary layer are weaker and less detectable due to uncertainties. The increase in boundary layer $NO_x$ concentrations led to an approximate 2.5 Tg $yr^{-1}$ increase in the $CH_4$ sink from 2005–2009 to 2015–2019. Free tropospheric $NO_x$ is estimated to have caused comparable decadal changes in global OH and $CH_4$ sink between 2005–2009 and 2015–2019 as boundary layer $NO_x$, though both have broad uncertainty ranges (Extended Data Fig. 2). The overall impact of tropospheric $NO_x$ is slightly larger than that of tropospheric CO but smaller than $H_2O_{(g)}$. However, the results for $NO_x$ should be interpreted with caution, as the division between boundary layer and free tropospheric $NO_x$ variations is subject to large uncertainties (Methods). The estimates for boundary layer $NO_x$ impacts over polluted regions tend to be more robust, such as the rising $NO_x$ burden over India (Extended Data Fig. 3) and the sharp decline globally during COVID-19 lockdowns (Extended Data Fig. 4). We thus focus on boundary layer $NO_x$ in the main text.

The increase in $TCO_3$ resulted in an approximate 1.5 Tg $yr^{-1}$ decrease in the $CH_4$ sink, though showing large uncertainty ranges that cross zero (Fig. 2g), Additionally, the increase in $CH_4$ itself caused a 5.6 Tg $yr^{-1}$ decadal decrease in the $CH_4$ sink by consuming more OH. This decrease is equivalent to about 25% of the increase in the $CH_4$ sink due to elevated atmospheric $CH_4$ mixing ratios (estimated with OH levels fixed at the 2005 level) during the same period.

**Spatial variations of OH and $CH_4$ sink**

The decadal changes in $[OH]_{trop\text{-}M}$ from the 2005–2009 mean to the 2015–2019 mean driven by key precursors are mapped at the grid scale to illustrate the spatial drivers across the globe and latitudinal bands, highlighting the resulting impacts on the chemical sink of $CH_4$ (Fig. 3).

The map shows the ensemble mean derived from various observational datasets and chemical mechanisms, representing the central estimate that reflects our best understanding.

The net increase of $[OH]_{trop\text{-}M}$ is concentrated in the tropical regions (30°S–30°N), reaching $2.0\times10^5$ molec $cm^{-3}$ across widespread areas (Fig. 3a). This increase is primarily driven by the rise in tropospheric $O_3$ and $H_2O_{(g)}$ (Figs. 3c and d). The results indicate a north-south asymmetry in OH increases, which is mainly attributed to the changes in CO concentration levels (Figs. 3b and g) and $H_2O_{(g)}$ (Figs. 3d and i). Reduced CO burdens have led to larger OH increases in the northern mid-latitude region, where North America, Europe, and China rapidly reduced their anthropogenic CO emissions through improved combustion efficiency of industrial boilers, residential stoves, and cars[33]. Due to the short lifetime of CO, emission reductions in the Northern Hemisphere can lead to uneven variations in OH levels between the two hemispheres. Meanwhile, $NO_x$ emissions and pollution have grown in South Asia, the Middle East, and North Africa, driving up OH levels in these regions (Fig. 3e). In contrast, $NO_x$ burden in North America, Western Europe, and East China declined over the corresponding period due to pollution control measures, curbing down OH levels. Due to the compensating influences from different regions across the Northern Hemisphere, $NO_x$ concentration changes within the boundary layer made only a small direct contribution to the north-south asymmetry in OH increases (Fig. 3j), as well as the indirect influences through $O_3$ formation.

The increase in the chemical sink of $CH_4$ also exhibits a north-south asymmetry, corresponding to the spatio-temporal variation patterns in OH (Fig. 3k). The $CH_4$ sink due to OH is estimated to have increased by 9.0 (3.6–15.6) Tg $yr^{-1}$ and 4.7 (−0.4–10.2) Tg $yr^{-1}$ in the northern and southern tropics, respectively, from the 2005–2009 mean to the 2015–2019 mean. In the northern mid-latitude band (30°N–60°N), the $CH_4$ sink increased by 3.3 (1.7–5.5) Tg $yr^{-1}$, while the increase was moderate (1.4 Tg $yr^{-1}$) in the southern mid-latitude (60°S–30°S). The substantial increase in the $CH_4$ sink over the tropics was driven by the increase in tropospheric $O_3$ and $H_2O_{(g)}$, accounting for approximately 9 Tg $yr^{-1}$ and 6 Tg $yr^{-1}$, respectively (Figs. 3m and n), of which 4 Tg $yr^{-1}$ was offset by the OH decrease due to the rising $CH_4$. The reduction in CO across the Northern Hemisphere increased $CH_4$ sink by about 3.5 Tg $yr^{-1}$ (Fig. 3l). The increase in chemical sink of $CH_4$ was also led by the increase in $H_2O_{(g)}$ over the Northern Hemisphere (5.3 Tg $yr^{-1}$), about 2.0 Tg $yr^{-1}$ greater than the Southern Hemisphere. Overall, the spatial patterns of the decadal increases in OH and the associated $CH_4$ sink reflect the influence of the global spatial-temporal redistribution of air pollutants across latitudinal bands, particularly regarding reduced CO and enhanced $O_3$ pollution, as well as the distribution of $H_2O_{(g)}$ increases due to climate change.

Air pollutant concentrations are influenced by precursor emissions from both natural sources (e.g., wildfires, soil, wetlands, lightning) and anthropogenic sources (e.g., energy, industry, transportation). These emissions exhibit interannual variations superimposed on long-term trends. Extreme events, such as megadroughts and economic recessions, can cause substantial disturbances in atmospheric compositions, offering a unique opportunity to understand the impacts of air pollutants on tropospheric OH and $CH_4$ sinks. Next, we focus on four anomalous years characterized by sudden changes in wildfire or human emissions to gain insights into short-term OH variations, drivers, and their impacts on the global $CH_4$ budget.

**Fire impacts during El Niño years**

The impacts of fire emissions on $CH_4$ sinks were separately analyzed for the periods 2008–2009 and 2015–2016, which represent contrasting phases of global fire activity. During 2008–2009, fire CO emissions were anomalously low following the multiyear La Niña event of 2007/2008[33]. This reduction in fire CO emissions led to a concurrent drop in global CO levels,

subsequently increasing the global $CH_4$ sink by 11.4 (8.9–14.2) Tg $yr^{-1}$ (Fig. 4a). This increase in $CH_4$ chemical sink due to decreased CO was evident across all latitude bands (Extended Data Fig. 5). Additionally, but smaller, an increase in $O_3$ over the tropics slightly contributed to the global $CH_4$ sink by 2.2 (1.1–3.5) Tg $yr^{-1}$ during this period. The global rise in OH levels and the associated $CH_4$ chemical sink during 2008–2009 was accompanied by a temporary slowdown in the atmospheric growth rate of $CH_4$ within those years (Fig. 1). This highlights the critical role of OH in shaping the interannual variation of the global $CH_4$ budget.

During 2015–2016, global fire emissions were extremely high due to intensified wildfires in the tropics, particularly from peatland burning in Southeast Asia driven by the El Niño event. This led to a large increase in CO concentrations over the tropics, resulting in a substantial weakening of the global $CH_4$ sink by 16.9 (12.9–21.3) Tg $yr^{-1}$ compared to the corresponding period before El Niño (Figs. 4b and and Extended Data Fig. 5). More than half of these negative anomalies were offset by an increase in the $CH_4$ sink driven by elevated $H_2O_{(g)}$ levels, around 10.0 Tg $yr^{-1}$, over the tropics. Meanwhile, wildfires directly released $CH_4$ emissions amounting to 4.4 (1.4–7.5) Tg $yr^{-1}$ positive anomalies[2], which is smaller than the reduction in $CH_4$ sink due to increased wildfire CO emissions contemporally. Both of these effects increase the global $CH_4$ burden, but the feedback loop involving fire CO emissions, OH levels, and $CH_4$ sink plays a more dominant role in regulating the global $CH_4$ budget than direct fire $CH_4$ emissions.

**Human impacts of the pandemic period**

The impacts of anthropogenic emissions on $CH_4$ sinks were also investigated for the years 2020 and 2021. During these years, the world was affected by COVID-19, and the lockdown measures implemented led to a sharp reduction in human activities and emissions[36]. The surface network observed an increase in the atmospheric growth rate of global $CH_4$ in 2020 and 2021, which are 5.8 ppb $yr^{-1}$ and 8.3 ppb $yr^{-1}$ higher than 2019, respectively[37] (Fig. 1b). Our estimations indicate a steady decline in global OH concentrations of $0.1–0.2\times10^5$ molec $cm^{-3}$ $yr^{-1}$ (1–2% $yr^{-1}$) from 2019 to 2021 (Fig. 1a). Compared to 2019 levels, the global chemical sink of $CH_4$ was estimated to have decreased by 11.0±3.5 Tg $yr^{-1}$ (based on MOZART) or 7.0±2.5 Tg $yr^{-1}$ (based on GEOS-Chem) in 2020 (Fig. 4c). In 2021, this decrease reached 15.6±4.3 Tg $yr^{-1}$ (MOZART) or 10.6±3.6 Tg $yr^{-1}$ (GEOS-Chem) compared to 2019 (Fig. 4d). These findings align with the previous atmospheric chemistry transport model simulations and top-down inversion of the HFC species and $CH_4$, which estimated an approximately 1.5% $yr^{-1}$ decrease in OH from 2019 to 2020[28,38,39]. This reduction is reported to account for 53±10% of the increase in $CH_4$ growth rate observed by the surface network in 2020 compared to 2019[28], and 14–34% based on the inversions of satellite observations[38,39].

The drop in OH and $CH_4$ sink in 2020 and 2021 was primarily attributed to the decline in tropospheric $O_3$ levels (Figs. 4c and d). This decline in $O_3$ was caused by reduced anthropogenic $NO_x$ emissions during the COVID-19 lockdown in 2020 and the incomplete recovery of emissions, such as those from air transport, in 2021[40]. These factors substantially restricted socioeconomic activities and associated emissions. Overall, the decrease in $O_3$ accounted for nearly 70% of the reduction in the global $CH_4$ chemical sink during these two years, with other precursors contributing to the remaining 30% decline. In 2020, elevated CO concentrations in the Southern Hemisphere due to intensive wildfires reduced the $CH_4$ sink, nearly matching the impacts of reduced $O_3$ concentrations in that region (Extended Data Fig. 5). The higher $TCO_3$ levels over the northern tropics also contributed to a decrease in the $CH_4$ sink (up to 3 Tg $yr^{-1}$) but were offset by lower $TCO_3$ levels over latitudes north of 30°N. In 2021, tropospheric $O_3$ levels remained comparable to those in 2020[41]. The enhanced CO concentrations north of 30°N due to extreme boreal forest fires[42] contributed to a small decrease

in $CH_4$ sink but was offset by the decline of CO south of 30°N. The additional decrease in $H_2O_{(g)}$ and increase in $TCO_3$ together led to a further decline in the $CH_4$ sink in 2021 (Fig. 4d).

During the COVID-19 period, anthropogenic $NO_x$ emissions declined for both surface sources and high-altitude aircraft sources, with the associated decline in tropospheric $O_3$ dominating the reduction in the global $CH_4$ sink. For OH production and loss directly resulting from changes in $NO_x$ concentrations, reduced $NO_x$ levels within the boundary layer led to a decrease in OH in North America and Europe, while causing a slight increase in high-$NO_x$ regions such as Eastern Asia (Extended Data Fig. 4). The free tropospheric $NO_x$ concentrations, influenced by emissions from aircraft, lightning, and the transport of $NO_x$ reservoirs such as peroxyacetyl nitrate (PAN)[43], are not well constrained in this study due to a lack of direct observations (Extended Data Fig. 6), while the influences on $O_3$ concentrations are evaluated separately.

**Balance air quality and climate concerns**

Reducing $CH_4$ emissions is the most crucial strategy for mitigating its climate impacts and addresses the indirect radiative forcing effects caused by $CH_4$ degradation products, which contribute to the production of greenhouse gases like $O_3$, stratospheric water vapor, and $CO_2$[1]. Mitigating $CH_4$ emissions is also recognized as an effective strategy for reducing peak warming from climate change due to $CH_4$'s much shorter atmospheric lifetime compared to $CO_2$[44]. However, it is essential to recognize that $CH_4$ concentration levels and their climate effects are controlled by both their sources and sinks[2], which are highly dependent on chemistry-climate feedback. For example, potential increases in natural $CH_4$ emissions, such as from permafrost thawing, have been recognized as major climate risks[45]. On the other hand, large uncertainties still exist in the chemical sink of $CH_4$[2].

We quantified in this paper how trends and variations in air pollution at both global and regional scales critically influence OH over decadal timescales, the primary atmospheric oxidant of $CH_4$, as shown by the conceptual diagram (Extended Data Fig. 7). Our study infers rising $O_3$ but decreasing CO due to changes in air pollution, have contributed to increase in OH levels and consumed more $CH_4$ in the atmosphere. This has buffered the rapid rise in anthropogenic $CH_4$ emissions observed over the past two decades, highlighting the critical influence of both natural and anthropogenic pollutant emission sources on the global $CH_4$ budget.

Learning from the past, one can expect that air quality regulations will critically affect the capability of OH to buffer $CH_4$ emissions. Particularly, $O_3$, which adversely impacts human health and ecosystems, is a regulated air pollutant worldwide[46,47]. Despite recent increases in atmospheric $O_3$ concentrations, efforts by many countries suggest that $O_3$ pollution could be mitigated in the future[34,48]. Reduced tropospheric $O_3$ implies less OH production and a reduced $CH_4$ chemical sink, similar to what occurred during the COVID-19 period in 2020 and 2021. This reduction in OH could drive up $CH_4$ concentrations without changes in $CH_4$ emissions.

In addition to $O_3$, CO emissions from intense wildfires also warrant attention. While CO emissions have declined since 2005 due to anthropogenic pollution control measures, global wildfire emissions remain high[33,49]. In some regions, such as boreal forests, wildfires have become more frequent and severe recently[42], increasingly influencing global CO trends and variations. Furthermore, global warming is likely to trigger more droughts, water deficits, and fire weather conditions, exacerbating wildfire activity[42]. The CO emissions from these probable wildfires will counteract the beneficial effects of air pollution cuts and pose a further threat to global OH levels and the $CH_4$ sink. Climate feedback with potentially positive effects on OH, on the other hand, may result from increased water vapor in the atmosphere[35] or an increase in stratosphere-troposphere transport of ozone[50].

The examples of $O_3$ and CO discussed above illustrate how air pollution regulations can alter the OH and $CH_4$ budgets. It is crucial to develop tools for monitoring and modeling OH levels both globally and regionally while continuing to implement effective air quality regulations to protect human health and the environment. The integrated observation- and model-driven system developed in this study represents an important effort to monitor OH levels. By regularly updating all driving factors, this system enables us to track spatial and temporal variations in OH levels, supporting the dynamic investigation of its influence on the global $CH_4$ budget. Addressing both air pollution and climate crisis requires a state-of-the-art, transparent, reliable understanding of the OH burden, which can underpin targeted and effective policies.

**References**


1 Szopa, S. *et al.* in *Climate Change 2021 – The Physical Science Basis: Working Group I Contribution to the Sixth Assessment Report of the Intergovernmental Panel on Climate Change* (ed Change Intergovernmental Panel on Climate) 817-922 (Cambridge University Press, 2023).

2 Saunois, M. *et al.* The Global Methane Budget 2000–2017. *Earth Syst. Sci. Data* **12**, 1561-1623, doi:10.5194/essd-12-1561-2020 (2020).

3 Rigby, M. *et al.* Renewed growth of atmospheric methane. *Geophysical Research Letters* **35**, L22805, doi:10.1029/2008gl036037 (2008).

4 Zhang, Z. *et al.* Anthropogenic emission is the main contributor to the rise of atmospheric methane during 1993–2017. *National Science Review* **9**, doi:10.1093/nsr/nwab200 (2021).

5 Zhang, Z. *et al.* Recent intensification of wetland methane feedback. *Nature Climate Change* **13**, 430-433, doi:10.1038/s41558-023-01629-0 (2023).

6 Qu, Z. *et al.* Inverse modeling of 2010–2022 satellite observations shows that inundation of the wet tropics drove the 2020–2022 methane surge. **121**, e2402730121, doi:doi:10.1073/pnas.2402730121 (2024).

7 Turner, A. J., Frankenberg, C. & Kort, E. A. Interpreting contemporary trends in atmospheric methane. *Proc. Natl. Acad. Sci. U.S.A.* **116**, 2805-2813, doi:10.1073/pnas.1814297116 (2019).

8 Lelieveld, J., Gromov, S., Pozzer, A. & Taraborrelli, D. Global tropospheric hydroxyl distribution, budget and reactivity. *Atmos. Chem. Phys.* **16**, 12477-12493, doi:10.5194/acp-16-12477-2016 (2016).

9 Kuklinska, K., Wolska, L. & Namiesnik, J. Air quality policy in the U.S. and the EU – a review. *Atmospheric Pollution Research* **6**, 129-137, doi:https://doi.org/10.5094/APR.2015.015 (2015).

10 Lelieveld, J., Gromov, S., Pozzer, A. & Taraborrelli, D. Global tropospheric hydroxyl distribution, budget and reactivity. *Atmospheric Chemistry and Physics* **16**, 12477-12493, doi:10.5194/acp-16-12477-2016 (2016).

11 Zhao, Y. *et al.* On the role of trend and variability in the hydroxyl radical (OH) in the global methane budget. *Atmos. Chem. Phys.* **20**, 13011-13022, doi:10.5194/acp-20-13011-2020 (2020).

12 Naik, V. *et al.* Preindustrial to present-day changes in tropospheric hydroxyl radical and methane lifetime from the Atmospheric Chemistry and Climate Model Intercomparison Project (ACCMIP). *Atmospheric Chemistry and Physics* **13**, 5277-5298, doi:10.5194/acp-13-5277-2013 (2013).

13 Voulgarakis, A. *et al.* Analysis of present day and future OH and methane lifetime in the ACCMIP simulations. *Atmospheric Chemistry and Physics* **13**, 2563-2587, doi:10.5194/acp-13-2563-2013 (2013).

14 Turner, A. J., Fung, I., Naik, V., Horowitz, L. W. & Cohen, R. C. Modulation of hydroxyl variability by ENSO in the absence of external forcing. *Proceedings of the National Academy of Sciences* **115**, 8931-8936, doi:10.1073/pnas.1807532115 (2018).
15 He, J., Naik, V. & Horowitz, L. W. Hydroxyl Radical (OH) Response to Meteorological Forcing and Implication for the Methane Budget. **48**, e2021GL094140, doi:https://doi.org/10.1029/2021GL094140 (2021).
16 Nicely, J. M. *et al.* A machine learning examination of hydroxyl radical differences among model simulations for CCMI-1. *Atmos. Chem. Phys.* **20**, 1341-1361, doi:10.5194/acp-20-1341-2020 (2020).
17 Duncan, B. N. *et al.* Opinion: Beyond global means – novel space-based approaches to indirectly constrain the concentrations of and trends and variations in the tropospheric hydroxyl radical (OH). *Atmos. Chem. Phys.* **24**, 13001-13023, doi:10.5194/acp-24-13001-2024 (2024).
18 Baublitz, C. B. *et al.* An observation-based, reduced-form model for oxidation in the remote marine troposphere. **120**, e2209735120, doi:doi:10.1073/pnas.2209735120 (2023).
19 Shutter, J. D. *et al.* Interannual changes in atmospheric oxidation over forests determined from space. **10**, eadn1115, doi:doi:10.1126/sciadv.adn1115 (2024).
20 Zhu, Q., Fiore, A. M., Correa, G., Lamarque, J.-F. & Worden, H. The impact of internal climate variability on OH trends between 2005 and 2014. *Environmental Research Letters* **19**, 064032, doi:10.1088/1748-9326/ad4b47 (2024).
21 Wolfe, G. M. *et al.* Mapping hydroxyl variability throughout the global remote troposphere via synthesis of airborne and satellite formaldehyde observations. *Proceedings of the National Academy of Sciences* **116**, 11171-11180, doi:10.1073/pnas.1821661116 (2019).
22 Anderson, D. C. *et al.* Technical note: Constraining the hydroxyl (OH) radical in the tropics with satellite observations of its drivers – first steps toward assessing the feasibility of a global observation strategy. *Atmos. Chem. Phys.* **23**, 6319-6338, doi:10.5194/acp-23-6319-2023 (2023).
23 Anderson, D. C. *et al.* Trends and Interannual Variability of the Hydroxyl Radical in the Remote Tropics During Boreal Autumn Inferred From Satellite Proxy Data. **51**, e2024GL108531, doi:https://doi.org/10.1029/2024GL108531 (2024).
24 Souri, A. H. *et al.* Enhancing long-term trend simulation of the global tropospheric hydroxyl (TOH) and its drivers from 2005 to 2019: a synergistic integration of model simulations and satellite observations. *Atmos. Chem. Phys.* **24**, 8677-8701, doi:10.5194/acp-24-8677-2024 (2024).
25 Pimlott, M. A. *et al.* Investigating the global OH radical distribution using steady-state approximations and satellite data. *Atmos. Chem. Phys.* **22**, 10467-10488, doi:10.5194/acp-22-10467-2022 (2022).
26 Nicely, J. M. *et al.* Changes in Global Tropospheric OH Expected as a Result of Climate Change Over the Last Several Decades. *Journal of Geophysical Research: Atmospheres* **123**, 10,774-710,795, doi:doi:10.1029/2018JD028388 (2018).
27 Rowlinson, M. J. *et al.* Impact of El Niño–Southern Oscillation on the interannual variability of methane and tropospheric ozone. *Atmos. Chem. Phys.* **19**, 8669-8686, doi:10.5194/acp-19-8669-2019 (2019).
28 Peng, S. *et al.* Wetland emission and atmospheric sink changes explain methane growth in 2020. *Nature* **612**, 477-482, doi:10.1038/s41586-022-05447-w (2022).
29 Naus, S. *et al.* Constraints and biases in a tropospheric two-box model of OH. *Atmos. Chem. Phys.* **19**, 407-424, doi:10.5194/acp-19-407-2019 (2019).

30 Patra, P. K. *et al.* Methyl Chloroform Continues to Constrain the Hydroxyl (OH) Variability in the Troposphere. *Journal of Geophysical Research: Atmospheres* **126**, e2020JD033862, doi:https://doi.org/10.1029/2020JD033862 (2021).
31 Thompson, R. L. *et al.* Estimation of the atmospheric hydroxyl radical oxidative capacity using multiple hydrofluorocarbons (HFCs). *Atmos. Chem. Phys.* **24**, 1415-1427, doi:10.5194/acp-24-1415-2024 (2024).
32 Zheng, B. *et al.* Rapid decline in carbon monoxide emissions and export from East Asia between years 2005 and 2016. *Environmental Research Letters* **13**, 044007, doi:10.1088/1748-9326/aab2b3 (2018).
33 Zheng, B. *et al.* Global atmospheric carbon monoxide budget 2000–2017 inferred from multi-species atmospheric inversions. *Earth Syst. Sci. Data* **11**, 1411-1436, doi:10.5194/essd-11-1411-2019 (2019).
34 Wang, H. *et al.* Global tropospheric ozone trends, attributions, and radiative impacts in 1995–2017: an integrated analysis using aircraft (IAGOS) observations, ozonesonde, and multi-decadal chemical model simulations. *Atmos. Chem. Phys.* **22**, 13753-13782, doi:10.5194/acp-22-13753-2022 (2022).
35 Held, I. M. & Soden, B. J. Water Vapor Feedback and Global Warming. **25**, 441-475, doi:https://doi.org/10.1146/annurev.energy.25.1.441 (2000).
36 Miyazaki, K. *et al.* Global tropospheric ozone responses to reduced NOx emissions linked to the COVID-19 worldwide lockdowns. **7**, eabf7460, doi:doi:10.1126/sciadv.abf7460 (2021).
37 Dlugokencky, E., Steele, L., Lang, P. & Masarie, K. The growth rate and distribution of atmospheric methane. *Journal of Geophysical Research: Atmospheres* **99**, 17021-17043, doi: https://doi.org/10.1029/94JD01245 (1994).
38 Feng, L., Palmer, P. I., Parker, R. J., Lunt, M. F. & Bösch, H. Methane emissions are predominantly responsible for record-breaking atmospheric methane growth rates in 2020 and 2021. *Atmos. Chem. Phys.* **23**, 4863-4880, doi:10.5194/acp-23-4863-2023 (2023).
39 Qu, Z. *et al.* Attribution of the 2020 surge in atmospheric methane by inverse analysis of GOSAT observations. *Environmental Research Letters* **17**, 094003, doi:10.1088/1748-9326/ac8754 (2022).
40 Steinbrecht, W. *et al.* COVID-19 Crisis Reduces Free Tropospheric Ozone Across the Northern Hemisphere. **48**, e2020GL091987, doi:https://doi.org/10.1029/2020GL091987 (2021).
41 Ziemke, J. R. *et al.* NASA Satellite Measurements Show Global-Scale Reductions in Free Tropospheric Ozone in 2020 and Again in 2021 During COVID-19. **49**, e2022GL098712, doi:https://doi.org/10.1029/2022GL098712 (2022).
42 Zheng, B. *et al.* Record-high CO2 emissions from boreal fires in 2021. **379**, 912-917, doi:doi:10.1126/science.ade0805 (2023).
43 Fischer, E. V. *et al.* Atmospheric peroxyacetyl nitrate (PAN): a global budget and source attribution. *Atmos. Chem. Phys.* **14**, 2679-2698, doi:10.5194/acp-14-2679-2014 (2014).
44 Shindell, D. *et al.* A climate policy pathway for near- and long-term benefits. **356**, 493-494, doi:doi:10.1126/science.aak9521 (2017).
45 Knoblauch, C., Beer, C., Liebner, S., Grigoriev, M. N. & Pfeiffer, E.-M. Methane production as key to the greenhouse gas budget of thawing permafrost. *Nature Climate Change* **8**, 309-312, doi:10.1038/s41558-018-0095-z (2018).
46 Unger, N., Zheng, Y., Yue, X. & Harper, K. L. Mitigation of ozone damage to the world's land ecosystems by source sector. *Nature Climate Change* **10**, 134-137, doi:10.1038/s41558-019-0678-3 (2020).

47 Fleming, Z. L. *et al.* Tropospheric Ozone Assessment Report: Present-day ozone distribution and trends relevant to human health. *Elementa: Science of the Anthropocene* **6**, doi:10.1525/elementa.273 (2018).
48 Organization, W. H. *WHO global air quality guidelines: particulate matter (PM2. 5 and PM10), ozone, nitrogen dioxide, sulfur dioxide and carbon monoxide*. (World Health Organization, 2021).
49 Zheng, B. *et al.* Increasing forest fire emissions despite the decline in global burned area. **7**, eabh2646, doi:doi:10.1126/sciadv.abh2646 (2021).
50 Hegglin, M. I. & Shepherd, T. G. Large climate-induced changes in ultraviolet index and stratosphere-to-troposphere ozone flux. *Nature Geoscience* **2**, 687-691, doi:10.1038/ngeo604 (2009).

## Methods

### General methodology

In this study, we developed an approach (Fig. S1) to estimate tropospheric OH concentrations ([OH]) and changes in the $CH_4$ sink from 2005 to 2021, focusing on the main OH precursors: tropospheric CO, $H_2O_{(g)}$, $O_3$, $CH_4$, $NO_x$, and total column $O_3$ ($TCO_3$). Building on the methods of previous studies[26] and our prior research[51], this approach integrated (I) 3D model simulations of atmospheric composition and meteorological conditions for 2005; (II) chemical box model experiments to estimate [OH] responses to changes in each precursor; and (III) quantifications of the main OH precursor changes during 2005–2021 based on observation-based datasets (Tables S1-3). We performed chemical box model experiments for each 3D model grid cell, driven by the atmospheric composition and meteorological conditions from 3D model simulations and observation-based datasets for the year 2005. These experiments allowed us to calculate the sensitivity of OH to varying extents of precursor concentration changes (OH sensitivity). We then determined the year-to-year variations in [OH] induced by the main precursors from 2005 to 2021 by combining the box model-calculated OH sensitivity with the observation-based OH precursor datasets.

To address uncertainties in OH chemistry, we employed two different chemical mechanisms (MOZART-4 and GEOS-Chem) for calculating OH sensitivity separately. For each precursor, we also utilized 2–4 observation datasets to quantify their interannual changes and represent potential uncertainties, which were derived from satellite retrievals (Table S1) and chemical reanalysis (Table S2). The data sources for the OH precursors used in this study are summarized in Table S3. The satellite-retrieved vertical column densities (VCDs) of tropospheric $O_3$ and $NO_2$ were converted into 3D distributions using vertical profiles simulated by 3D models. The influence of tropospheric $O_3$ and $NO_x$ on OH was estimated across altitudes by vertical layers. In regions dominated by anthropogenic surface sources, boundary layer $NO_2$ variations can be inferred with greater confidence from total tropospheric column data[52]. While free tropospheric $NO_x$ contributes to the total tropospheric $NO_x$ burden and OH variations[53,54], accurately assessing its impact on OH requires reliable vertical profiles and their temporal evolution—data that are currently unavailable. The annual scale impacts of free tropospheric $NO_x$ are less well constrained in this study and tend to be more uncertain than those of the other species analyzed. Therefore, for the influence of $NO_x$ on [OH] and $CH_4$ loss, we focus on the results for boundary layer $NO_x$ in the main text and show the magnitudes of free tropospheric $NO_x$ impacts in the Extend Data Figs. 2 and 6.

The overall interannual variations of [OH] and $CH_4$ loss were determined by summing the [OH] changes induced by individual precursors. We applied the Monte Carlo method to randomly sample the changes in tropospheric [OH] and $CH_4$ chemical loss driven by each OH precursor,

estimated from different observations. This approach allowed us to derive the mean values and the uncertainty range of the overall interannual variations. To examine the additivity of the [OH] changes due to different precursors, we used a chemical box model to simulate [OH] under three conditions in our previous study[51]: (I) using 3D model outputs ($[OH]_{model}$); (II) simultaneously replacing the major OH precursors with observation-based data ($[OH]_{obs}$); and (III) individually replacing each OH precursor ***Xk*** to observation-based data ($[OH]_{obs\_xk}$). We found that the [OH] changes caused by perturbing all major precursors together, as the difference between [OH] simulated by (I) and (II) ($[OH]_{diff\_1} = [OH]_{model} - [OH]_{obs}$), are consistent with those calculated by summing the differences between (I) and each (III) ($[\mathrm{OH}]_{diff\_2} = \sum([OH]_{model} - [OH]_{obs\_xk})$) (Fig.S2). Therefore, summing the [OH] changes from individual precursors is a valid approach for diagnosing overall [OH] changes on both global and 30° latitude band scales.

**The 3D model simulated OH precursors**

The 3D distributions of atmospheric trace gases and meteorological conditions to drive chemical box model simulations were from the IGAC/SPARC Chemistry-Climate Model Initiative Phase-1 (CCMI-1)[55]. We used the outputs from REF-C1 experiments, which were simulated by the Community Earth System Model (CESM) using the Community Atmosphere Model version 4 as an atmosphere component (CESM1 CAM4-chem)[56] and the GEOS-5 Chemistry Climate Model (GEOSCCM)[57-59].

The REF-C1 experiments were driven by observation-based sea surface temperature and state-of-the-art historical forcing from 1960 to 2010. The anthropogenic emissions of REF-C1 experiments were derived from the MACCity inventory[60]. The model simulations also included natural emissions from biomass burning, lightning, and biogenic sources[55]. The tropospheric gas-phase chemistry of CESM1 CAM4-chem is mostly based on the MOZART-4 mechanisms. The tropospheric chemistry of GEOSCCM is from the chemistry Global Modeling Initiative (GMI) combined tropospheric-stratospheric chemical mechanism[61,62]. For a detailed description of CCMI model and experiments information regarding the tropospheric OH concentrations and OH precursors simulated by CESM1 CAM4-chem and GEOSCCM can be found in previous studies [63,51,55].

**The chemical box model DSMACC experiments**

We calculated the responses in tropospheric [OH] to the aforementioned precursor changes using the Dynamically Simple Model of Atmospheric Chemical Complexity (DSMACC)[64]. This chemical box model generates code for a selected chemical mechanism via the Kinetic PreProcessor (KPP) and estimates the clear-sky photolysis rates using the tropospheric ultraviolet and visible (TUV) radiation model. Unlike the 3D atmospheric chemistry models that are usually driven by emission inventories, the DSMACC model is driven by the concentrations of chemical species, which are more easily constrained by observation-based datasets. Within the DSMACC framework, NO and $NO_2$ are treated as the $NO_x$ family and can be constrained by $NO_2$ concentrations.

In this study, we conducted the DSMACC model simulations with MOZART-4 and GEOS-Chem chemical mechanisms, respectively. The DSMACC simulations with MOZART-4 chemical mechanisms were driven by the chemical species concentrations and meteorological conditions from the outputs of CESM1 CAM4-chem of CCMI REF-C1 experiments, and the simulations with GEOS-Chem chemical mechanisms are driven by outputs of GEOSCCM. As demonstrated by our prior research[51], the DSMACC model was able to reproduce the spatial distributions of $[OH]_{trop\text{-}M}$ simulated by the corresponding 3D model, validating its ability to capture the response of [OH] to meteorological conditions and precursor concentrations.

For each chemical mechanism, we conducted the following DSMACC experiments:

(1) ***Ref_model*** experiment: Simulated [OH] ($[OH]_{DSMACC\_Ref\_model}$) with all DSMACC inputs taken directly from 3D atmospheric chemistry model simulations for each month in 2005.

(2) ***Obs_Xk_Ln*** experiments: Similar to the ***Ref_model*** experiment but the concentration of one individual OH precursor ***Xk*** (***X₁***=*CO*, ***X₂***=$H_2O_{(g)}$, ***X₃***=$O_3$, ***X₄***=$CH_4$, ***X₅***= $NO_2$, ***X₆***=$TCO_3$) was adjusted to ***Ln***% of the mean value observation-based datasets in 2005. Considering the nonlinear responses of [OH] to precursor concentrations, most precursors were increased in 20% increments from 20% to 200% (***L₁***=*20*, ***L₂***=*40,…*, ***L₁₀***=*200*). For $TCO_3$, ***Ln***% was increased by 10% step from 80% to 110% (***L₁***=*80*, ***L₂***=*90*, ***L₃***=*100*, ***L₄***=*110*). For $CH_4$, ***Ln***% was increased by 5% step from 95% to 105% (***L₁***=*95*, ***L₂***=*100*, ***L₃***=*105*).

To better represent the heterogeneous spatial-temporal distribution of OH, the DSMACC model experiments (***Ref_model*** and ***Obs_Xk_Ln)*** were conducted for each pixel of the 3D model grid in the troposphere (e.g., 144 (longitudes)×96 (latitudes)×13 (pressure levels) for CESM1 CAM4-chem grid) for each month using MOZART and GEOS-Chem chemical mechanisms.

**[OH] changes relative to 2005 induced by each precursor**

We calculated the [OH] changes between year ***y*** and 2005 due to each precursor ***Xk*** by multiplying the 3D model simulated baseline [OH] concentrations for 2005 ($[OH]_{model}$) with the relative [OH] changes generated from the DSMACC model experiments:

$$\delta[\mathrm{OH}]_{\mathrm{Xk\_y}} = [\mathrm{OH}]_{\mathrm{model}} \times \left( \frac{[\mathrm{OH}]_{\mathrm{DSMACC\_Xk\_y}} - [\mathrm{OH}]_{\mathrm{DSMACC\_Xk\_2005}}}{[\mathrm{OH}]_{\mathrm{DSMACC\_Ref\_model}}} \right) \quad (1)$$

Where $[OH]_{DSMACC\_ref\_model}$ is the [OH] simulated by ***Ref_model*** experiments of the DSMACC model; $[OH]_{DSMACC\_Xk\_2005}$ and $[OH]_{DSMACC\_Xk\_y}$ are the [OH] simulated by the DSMACC model with concentrations of precursor ***Xk*** perturbed to the observation-based values for 2005 and year ***y***, respectively. We did not directly use the absolute values of the DSMACC model simulated [OH] because the [OH] simulated by ***Ref_model*** experiments tended to overestimate [OH] by ~10–30% compared with corresponding 3D model simulations[51].

For each year ($y$ = 2005, 2006 ,…, 2021) and each observation-based dataset, calculating $[OH]_{DSMACC\_Xk\_y}$ requires numerous DSMACC simulations. To balance the computing cost and the nonlinearities in OH chemistry, we ran the ***Obs_Xk_Ln,*** which adjusted the concentrations of ***Xk*** to ***Ln***% of the multi-observation mean values of 2005 ($C_{Xk\_Ln}$). For each of the individual OH precursors ***Xk*** and each year ***y***, we searched for the $C_{Xk\_Ln}$ (n=N) that was closest to the observation-based concentrations ($C_{Xk\_y}$). We assume a linear response of [OH] to a small perturbation of ***Xk*** from $C_{Xk\_Ln}$ (n=N) to $C_{Xk\_y}$, and calculate the $[OH]_{DSMACC\_Xk\_y}$ by equation (2):

$$[\mathrm{OH}]_{\mathrm{DSMACC\_Xk\_y}} \approx [\mathrm{OH}]_{\mathrm{DSMACC\_Ref\_model}} + \left( [\mathrm{OH}]_{\mathrm{DSMACC\_Xk\_Ln}} - [\mathrm{OH}]_{\mathrm{DSMACC\_Ref\_model}} \right) \times \left( \frac{C_{\mathrm{Xk\_y}} - C_{\mathrm{Xk\_model}}}{C_{\mathrm{Xk\_Ln}} - C_{\mathrm{Xk\_model}}} \right) (\mathrm{n} = \mathrm{N}) \quad (2)$$

Where $C_{Xk\_model}$ is ***Xk*** concentrations simulated by the 3D model for 2005, $[OH]_{DSMACC\_Xk\_Ln}$ is the [OH] simulated by ***Obs_Xk_Ln*** (n=N).

**The $[OH]_{trop\text{-}M}$ and chemical loss of $CH_4$**

The changes in global and regional mean tropospheric column-averaged air-mass-weighted

OH concentration ($[OH]_{trop\text{-}M}$) caused by precursor ***Xk*** in year ***y***, relative to 2005 ($\delta[OH]_{Xk\_y}$) were calculated as:

$$\delta[\mathrm{OH}]_{\mathrm{trop-M}} = \frac{\sum_i \delta[\mathrm{OH}]_{\mathrm{Xk\_y}} \times \mathrm{m}}{\sum_i \mathrm{m}} \quad (3)$$

Where ***i*** is the index of the model grid cell in the troposphere and ***m*** is the corresponding air mass.

The changes in chemical loss of $CH_4$ through reaction with OH were calculated as:

$$\delta \mathrm{L}_{\mathrm{CH_4+OH}} = \sum_i \sum_t \mathrm{K}(\mathrm{T_a}) \times \mathrm{m}_{\mathrm{CH_4}} \times \delta[\mathrm{OH}]_{\mathrm{Xk\_y}} \delta \mathrm{t} \quad (4)$$

Where $\delta t$ is the monthly integration time step. The 3D $CH_4$ mass ($m_{CH4}$) distributions in 2005 are from the CAMS reanalysis. The $K(T_a)$ is the reaction rate of $CH_4$ with OH and was calculated as a function of air temperature ($T_a$)[65]:

$$\mathrm{K}(\mathrm{T_a}) = 2.45 \times 10^{-12} \mathrm{e}^{-\frac{1775}{\mathrm{T_a}}} \quad (5)$$

Where the distribution of $T_a$ was taken from the MERRA-2 reanalysis data.

For each OH precursor, we estimated $\delta[OH]_{trop\text{-}M}$ and $\delta\ L_{CH4+OH}$ using two different chemical mechanisms and multiple observation-based datasets.

**Box model for diagnosing the influence of $CH_4$ emissions on OH**

In the years such as 2007, 2014, 2015, 2020, and 2021, we observed negative anomalies in global $[OH]_{trop\text{-}M}$ coinciding with increased $CH_4$ growth rates compared to adjacent years. To investigate whether surges in $CH_4$ emissions could drive increases in $CH_4$ mixing ratios and subsequent decreases in global [OH], we developed a global box model, which operates on an hourly timestep and incorporates the following processes.

**(1) $CH_4$ emissions.** $CH_4$ emissions are converted into an incremental increase in the tropospheric $CH_4$ mixing ratio.

**(2) $CH_4$ losses.** $CH_4$ loss through the reaction with OH is calculated based on the tropospheric $CH_4$ mixing ratio and [OH]. Losses due to stratospheric processes (51 Tg $yr^{-1}$) and reactions with Cl (25 Tg $yr^{-1}$) are prescribed in the box model simulations, following an ensemble estimate of the global $CH_4$ budget[2].

**(3) OH response to $CH_4$ changes.** A 1 ppbv increase in tropospheric $CH_4$ leads to a decrease of $0.0018\times10^5$ molec $cm^{-3}$ in global mean [OH], derived from our chemical box model experiments (Fig. 2). This is consistent with ensemble 3D atmospheric chemistry model simulations, which show that a 960 ppbv increase in $CH_4$ corresponds to a 17.3±2.3% (~$1.73 \times 10^5$ molec $cm^{-3}$) decrease in [OH][12].

Initial conditions were set with a tropospheric $CH_4$ mixing ratio of 1800 ppbv and [OH] at $10^6$ molec $cm^{-3}$. $CH_4$ chemical loss through OH was estimated at 474 Tg $yr^{-1}$. To balance $CH_4$ loss (including OH, Cl, and stratospheric losses), we set initial $CH_4$ source emissions to 550 Tg $yr^{-1}$, establishing a steady state for both $CH_4$ and OH. In the fifth year of the simulation, we introduced a 10% increase in $CH_4$ annual emissions (55 Tg $yr^{-1}$)—a magnitude much larger than the decadal increase in global anthropogenic emissions from 2005–2009 to 2015–2019

(Fig. 2) and greater than typical interannual variations in wetland emissions (within ±10 Tg $yr^{-1}$)[66].

As shown in Fig. S3, this unrealistic surge in $CH_4$ emissions caused an increase in the global $CH_4$ annual growth rate of 23 ppbv $yr^{-1}$—larger than historical $CH_4$ annual growth rates in any year since 1985 (mostly below 10 ppbv $yr^{-1}$). However, the corresponding decrease in [OH] was only 0.4% $yr^{-1}$ ($0.04 \times 10^5$ molec $cm^{-3}$ $yr^{-1}$). This is less than half of the observed decreases in [OH] ($0.1–0.2\times10^5$ molec $cm^{-3}$ $yr^{-1}$) during years with significant negative anomalies, such as 2007, 2014, 2015, 2020, and 2021 (Fig. 1). These results suggest that $CH_4$ emissions are unlikely to be a primary driver of [OH] variations through perturbations in $CH_4$ abundance. Instead, interannual [OH] variations are predominantly influenced by reactive species such as CO, $O_3$, $NO_x$, and $H_2O_{(g)}$.

**Impacts of formaldehyde and isoprene on OH variations**

Formaldehyde ($CH_2O$) has a long-term satellite dataset (e.g., OMI) and has been used as a proxy for assessing OH variations, particularly in remote regions where $CH_2O$ is primarily produced from OH oxidation of $CH_4$[21]. However, $CH_2O$ is not a primary driver of OH changes, and its direct impact on global OH burden is limited. It accounts for only about 6% of the global OH sink[11], serving more as an indicator of the oxidation of NMVOCs by OH rather than directly influencing OH chemistry.

To evaluate $CH_2O$'s impact on global OH, we conducted an additional model experiment using global 3D $CH_2O$ distributions (2005–2017) derived from a variational atmospheric inversion system assimilating OMI v3 $CH_2O$ total column data[33]. Our results suggest that $CH_2O$ contributes to a minor decrease in global tropospheric [OH] of less than $0.05\times10^5$ molec $cm^{-3}$ (~0.5%) over the studied period (Fig. S4). Given these marginal effects and the lack of multiple reliable observation datasets, we chose not to include $CH_2O$ in our analysis, as its omission does not significantly affect the analysis of overall trends and drivers of global OH variations.

The impact of isoprene on [OH] variations is primarily observed in regions with high isoprene emissions, such as tropical forests, where atmospheric HCHO is primarily produced through the oxidation of isoprene[67,68]. Recent isoprene observations from the Cross-track Infrared Sounder (CrIS) satellite, spanning from February 2012 to December 2020, provide valuable data over forest regions of East Amazonia, New Guinea, and the Southeastern United States[19]. We used these CrIS data to assess the influence of isoprene on tropospheric [OH] variations in these regions. Our results indicate that isoprene contributes to 1%-3% of the interannual variations in regional $[OH]_{trop\text{-}M}$, with impacts comparable to those of CO and $O_3$ (Fig. S5). In our previous study, we estimated that isoprene accounts for 6% of the global OH sink [11]. However, fully quantifying the global impact of isoprene, along with other NMVOCs, requires long-term, global-scale observations of individual NMVOC species. Due to the absence of such data at the global scale, we focused on regional analysis in this study and did not incorporate isoprene into our global framework.

**Data availability**

The atmospheric composition concentrations simulated by GEOSCCM and CESM-CAM4Chem were downloaded from https://data.ceda.ac.uk/badc. The atmospheric methane growth rate data was obtained from https://gml.noaa.gov/ccgg/trends_ch4/. The CAMS EAC4 chemical reanalysis and EGG4 were downloaded from https://www.ecmwf.int/en/research/climate-reanalysis/cams-reanalysis. The TCR-2 chemical reanalysis data was downloaded from https://tes.jpl.nasa.gov/tes/chemical-reanalysis/. The

MERRA2 reanalysis data was downloaded from https://gmao.gsfc.nasa.gov/reanalysis/MERRA-2. The ERA5 reanalysis data was downloaded from https://www.ecmwf.int/en/forecasts/dataset/ecmwf-reanalysis-v5. The satellite tropospheric $O_3$ column was downloaded from https://acd-ext.gsfc.nasa.gov/Data_services/cloud_slice/new_data.html. The total $O_3$ column was downloaded from https://acd-ext.gsfc.nasa.gov/Data_services/merged/instruments.html. The QA4ECV tropospheric $NO_2$ product was downloaded from https://www.temis.nl/airpollution/no2.php. The NASA tropospheric $NO_2$ products were downloaded from https://disc.gsfc.nasa.gov/datasets/OMNO2d_003/summary. The global gridded distribution of the OH changes relative to 2005 due to individual OH precursors and the source data for the figures are available at Figshare (https://figshare.com/s/6ab4b1e5c20657b93279).

## Code availability

Code and documentation for the Chemical box model DSMACC are available at https://github.com/barronh/DSMACC.

## References


51 Zhao, Y. et al. Reconciling the bottom-up and top-down estimates of the methane chemical sink using multiple observations. Atmos. Chem. Phys. 23, 789-807, doi:10.5194/acp-23-789-2023 (2023).

52 Geddes, J. A., Martin, R. V., Boys, B. L. & Donkelaar, A. v. Long-Term Trends Worldwide in Ambient NO2 Concentrations Inferred from Satellite Observations. **124**, 281-289, doi:doi:10.1289/ehp.1409567 (2016).

53 Anderson, D. C. *et al.* Spatial and temporal variability in the hydroxyl (OH) radical: understanding the role of large-scale climate features and their influence on OH through its dynamical and photochemical drivers. *Atmos. Chem. Phys.* **21**, 6481-6508, doi:10.5194/acp-21-6481-2021 (2021).

54 Shah, V. *et al.* Nitrogen oxides in the free troposphere: implications for tropospheric oxidants and the interpretation of satellite NO2 measurements. *Atmos. Chem. Phys.* **23**, 1227-1257, doi:10.5194/acp-23-1227-2023 (2023).

55 Morgenstern, O. *et al.* Review of the global models used within phase 1 of the Chemistry–Climate Model Initiative (CCMI). *Geoscientific Model Development* **10**, 639-671, doi:10.5194/gmd-10-639-2017 (2017).

56 Tilmes, S. *et al.* Representation of the Community Earth System Model (CESM1) CAM4-chem within the Chemistry-Climate Model Initiative (CCMI). *Geosci. Model Dev.* **9**, 1853-1890, doi:10.5194/gmd-9-1853-2016 (2016).

57 Molod, A., Takacs, L., Suarez, M. & Bacmeister, J. Development of the GEOS-5 atmospheric general circulation model: evolution from MERRA to MERRA2. *Geosci. Model Dev.* **8**, 1339-1356, doi:10.5194/gmd-8-1339-2015 (2015).

58 Oman, L. D. *et al.* The ozone response to ENSO in Aura satellite measurements and a chemistry-climate simulation. *Journal of Geophysical Research: Atmospheres* **118**, 965-976, doi:https://doi.org/10.1029/2012JD018546 (2013).

59 Nielsen, J. E. *et al.* Chemical mechanisms and their applications in the Goddard Earth Observing System (GEOS) earth system model. *Journal of advances in modeling earth systems* **9**, 3019-3044 (2017).

60 Granier, C. *et al.* Evolution of anthropogenic and biomass burning emissions of air pollutants at global and regional scales during the 1980–2010 period. *Climatic Change* **109**, 163 (2011).

61 Duncan, B. N., Strahan, S. E., Yoshida, Y., Steenrod, S. D. & Livesey, N. Model study of the cross-tropopause transport of biomass burning pollution. *Atmos. Chem. Phys.* **7**, 3713-3736, doi:10.5194/acp-7-3713-2007 (2007).
62 Horowitz, L. W., Liang, J., Gardner, G. M. & Jacob, D. J. Export of reactive nitrogen from North America during summertime: Sensitivity to hydrocarbon chemistry. **103**, 13451-13476, doi:https://doi.org/10.1029/97JD03142 (1998).
63 Zhao, Y. *et al.* Inter-model comparison of global hydroxyl radical (OH) distributions and their impact on atmospheric methane over the 2000–2016 period. *Atmos. Chem. Phys.* **19**, 13701-13723, doi:10.5194/acp-19-13701-2019 (2019).
64 Emmerson, K. M. & Evans, M. J. Comparison of tropospheric gas-phase chemistry schemes for use within global models. *Atmos. Chem. Phys.* **9**, 1831-1845, doi:10.5194/acp-9-1831-2009 (2009).
65 Sander, S. P. *et al.* Chemical kinetics and photochemical data for use in atmospheric studies evaluation number 17. (Pasadena, CA: Jet Propulsion Laboratory, National Aeronautics and Space Administration, 2011, 2011).
66 Zhang, Z. *et al.* Enhanced response of global wetland methane emissions to the 2015–2016 El Niño-Southern Oscillation event. *Environmental Research Letters* **13**, 074009, doi:10.1088/1748-9326/aac939 (2018).
67 Wells, K. C. *et al.* Satellite isoprene retrievals constrain emissions and atmospheric oxidation. *Nature* **585**, 225-233, doi:10.1038/s41586-020-2664-3 (2020).
68 Wells, K. C. *et al.* Next-Generation Isoprene Measurements From Space: Detecting Daily Variability at High Resolution. **127**, e2021JD036181, doi:https://doi.org/10.1029/2021JD036181 (2022).
69 Crippa, M. *et al.* GHG emissions of all world countries. (2021).
70 Hoesly, R. M. *et al.* Historical (1750–2014) anthropogenic emissions of reactive gases and aerosols from the Community Emissions Data System (CEDS). *Geosci. Model Dev.* **11**, 369-408, doi:10.5194/gmd-11-369-2018 (2018).

**Acknowledgments**
The study was supported by the National Natural Science Foundation of China (grant numbers 42305101, 42375096, and 22188102).

**Author contributions**
B.Z. and Y.Z. designed and conceptualized the study. Y.Z. performed DSMACC simulations and created the figures. B.Z. and Y. Z. wrote the original draft. M.S., P.C., M.I.H., S.L., Y.L., and P.B. reviewed and commented on the manuscript.

**Competing interests**
The authors declare that they have no competing interests.

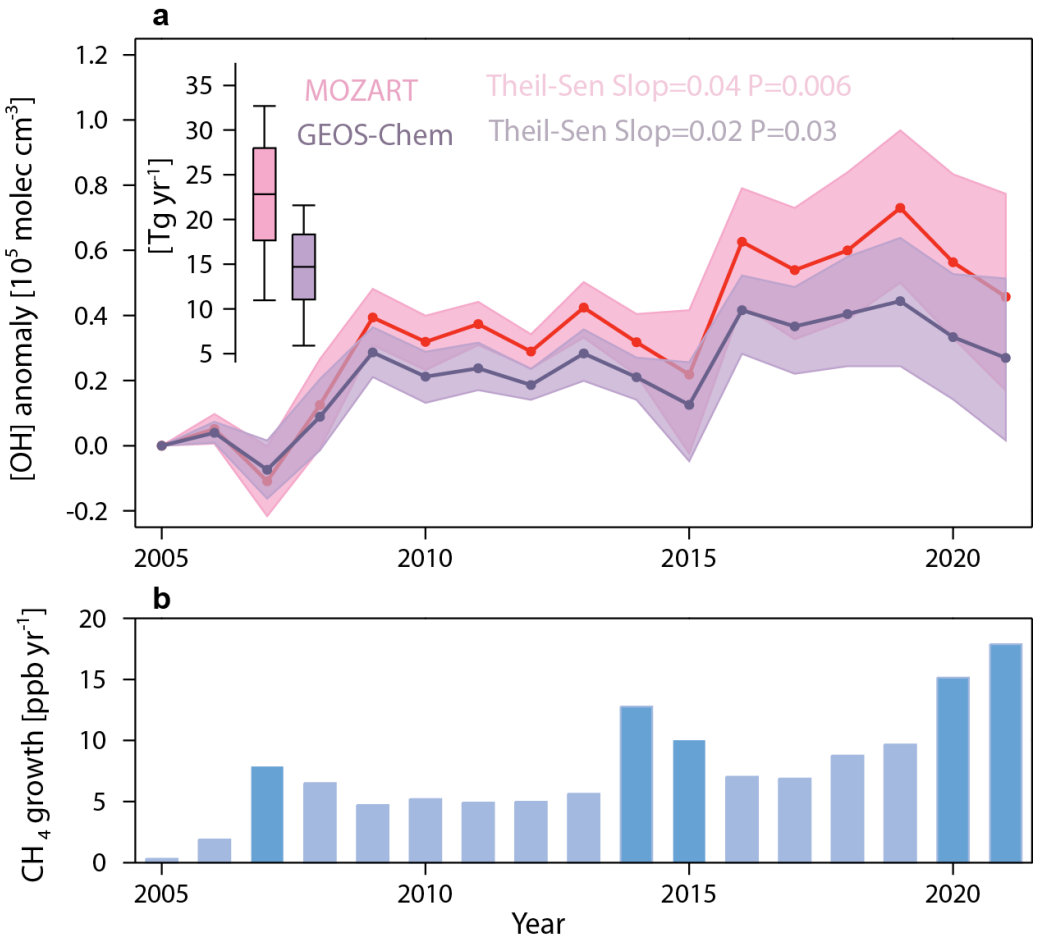


**Figure 1. Year-to-year variations in tropospheric OH concentrations and $CH_4$ growth rates.** (**a**) Net changes in global mean tropospheric OH concentrations ($[OH]_{trop\text{-}M}$) relative to 2005, driven by variations in tropospheric CO, $O_3$, $H_2O_{(g)}$, $CH_4$, boundary layer $NO_x$, and total column $O_3$ ($TCO_3$), as estimated using the MOZART (pink line) and GEOS-Chem (purple line) chemical mechanisms. The solid line represents the mean change in $[OH]_{trop\text{-}M}$, with the shaded areas indicating the uncertainty range based on different observation-based datasets. The inset displays the Theil-Sen slope of the mean $[OH]_{trop\text{-}M}$ changes, along with the P-value determined using the Mann-Kendall test. The whisker chart illustrates decadal changes (2005–2009 vs. 2015–2019) in the $CH_4$ sink driven by OH variations, showing the mean, standard deviation, and range. (**b**) $CH_4$ growth rates from the NOAA/GML observational network[37].

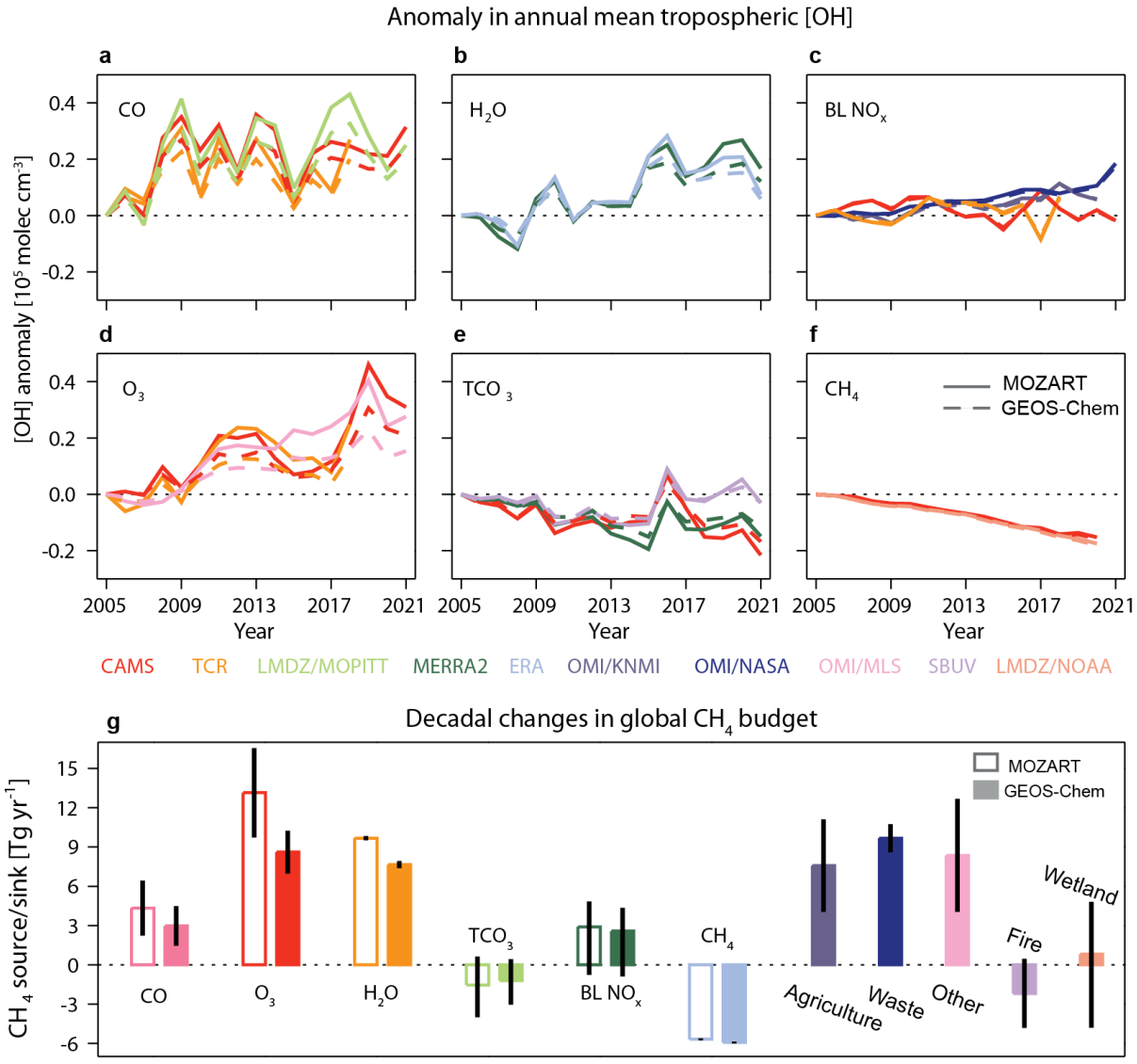


**Figure 2. Global tropospheric [OH] and $CH_4$ sink changes driven by individual OH precursors.** (**a–f**) Changes in global mean tropospheric OH concentrations ($[OH]_{trop\text{-}M}$) relative to 2005, driven by individual observation-based precursors. (**g**) Decadal changes (between 2005–2009 and 2015–2019) in the global $CH_4$ sink attributed to individual OH precursors, anthropogenic $CH_4$ emissions from agriculture, waste, and other sources as provided by the EDGARv7.0[69] and CEDSv2021_04_21[70] inventories, and bottom-up estimates of fire and wetland from the last Global Methane budget (between 2005–2009 and 2013–2017)[2]. The error bars represent the range of $CH_4$ source/sink estimates across different datasets. BL $NO_x$ refer to the $NO_x$ in boundary layer.

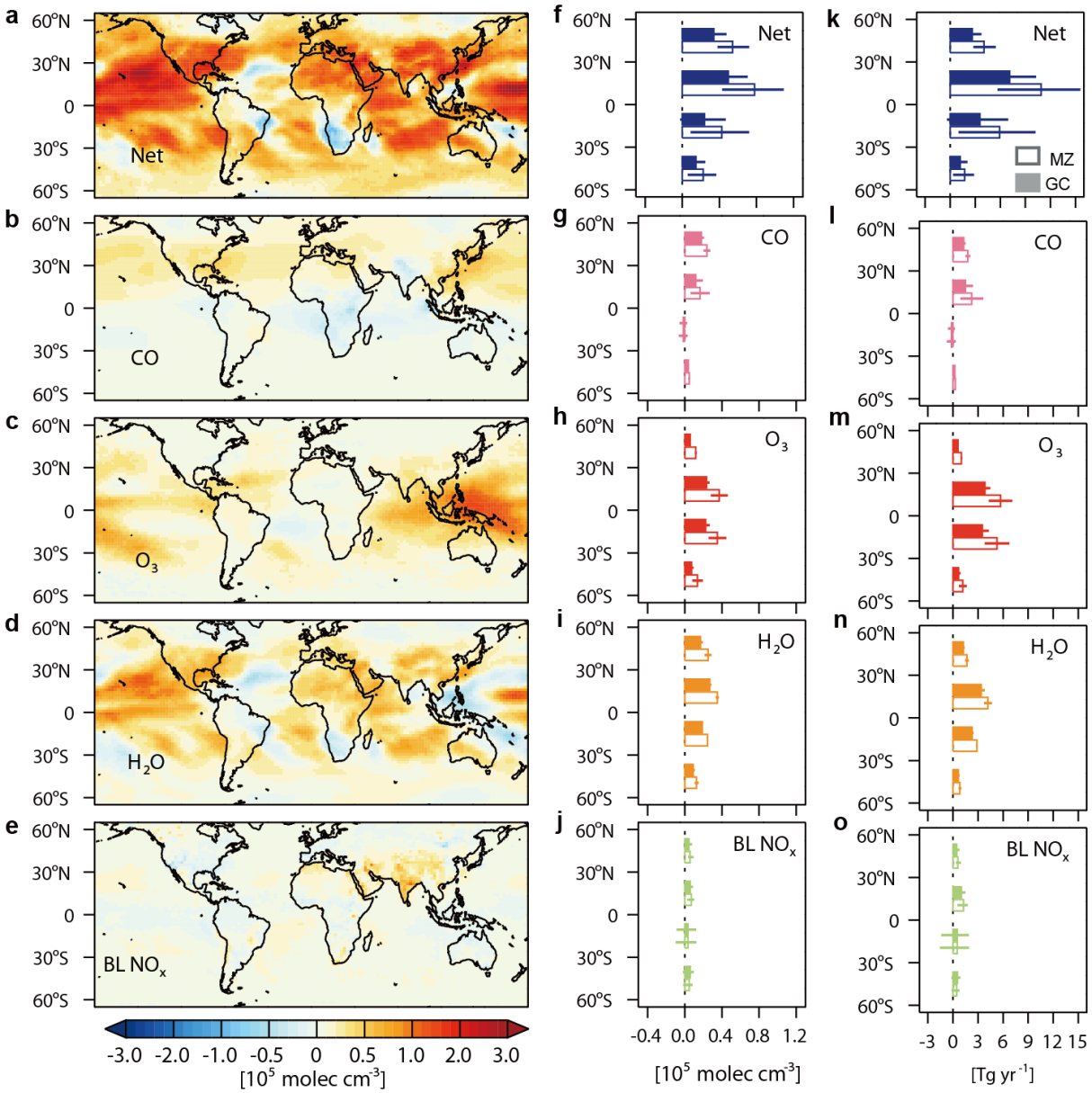


**Figure 3. Spatial distribution of decadal changes in tropospheric [OH] and $CH_4$ sink.** (**a–e**) Spatial patterns of decadal changes in mean tropospheric OH concentrations ($[OH]_{trop\text{-}M}$) driven by individual and total contributions from six OH precursors, as estimated by different observation-based datasets and two chemical mechanisms (MZ: MOZART, GC: GEOS-Chem). (**f–j**) Corresponding latitudinal changes in $[OH]_{trop\text{-}M}$. (**k–o**) Latitudinal changes in the chemical sink of $CH_4$. Error bars represent the range of $[OH]_{trop\text{-}M}$ and $CH_4$ sink estimates derived from various datasets.

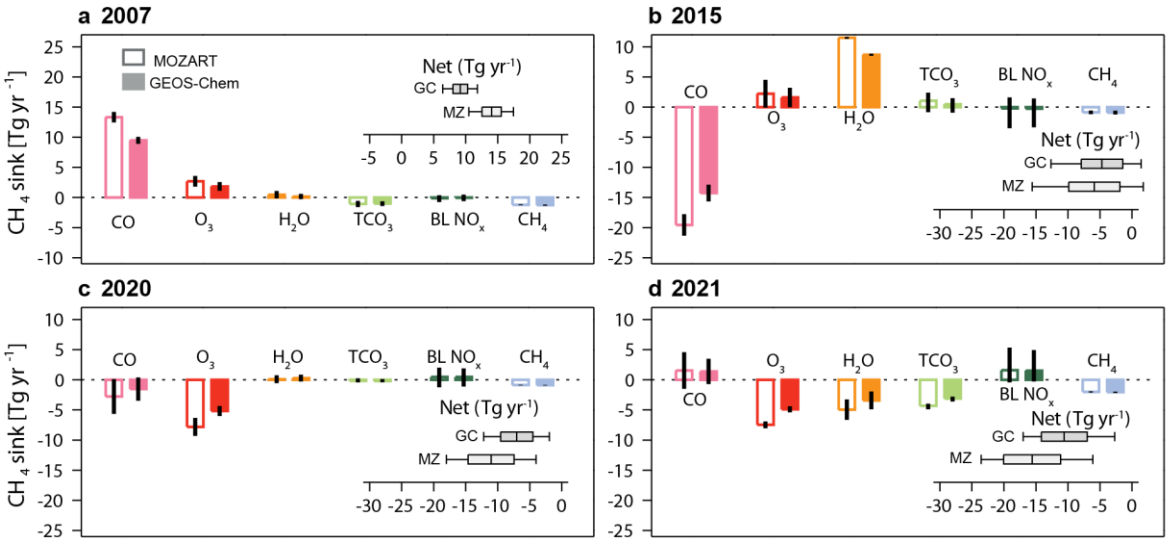


**Figure 4. Contributions of individual OH precursors to global $CH_4$ sink changes during unusual years.** (**a**) The rapid increase in the global $CH_4$ sink following 2007 (mean values of 2008–2009 minus 2006–2007). (**b**) Anomaly in the global $CH_4$ sink during the El Niño event starting in 2015 (mean values of 2015.5-2016.4 minus 2014.5-2015.4). (**c–d**) Anomalies in the global $CH_4$ sink during the COVID-19 lockdown in 2020 (2020 minus 2019) and 2021 (2021 minus 2019). Error bars represent the range of $CH_4$ sink estimates from various datasets. The whisker chart in the inset shows net anomalies estimated by the MOZART (MZ) and GEOS-Chem (GC) mechanisms.

## Extended data figures

**Extended Data Figure 1. Comparison of the global tropospheric mean [OH] with MCF-based and HFC-based inversions.** Tropospheric [OH] variations calculated using MOZART (pink) and GEOS-Chem (purple) chemical mechanisms are compared with MCF-based inversions from the 3D model as described by Patra et al.[30] and by Naus et al.[29] as well as with HFC-based inversions from the box model as described by Thompson et al.[32].

**Extended Data Figure 2. Contributions of $NO_x$ from the free troposphere to interannual variation of global $[OH]_{trop\text{-}M}$ and decadal changes in and chemical loss of $CH_4$.** (a) Interannual variations of $[OH]_{trop\text{-}M}$. (b)Decadal changes in chemical loss of $CH_4$.

**Extended Data Figure 3. Contributions of individual OH precursors to decadal changes in tropospheric [OH] in South Asia.** (a–c) Spatial patterns of decadal changes in mean tropospheric OH concentrations ($[OH]_{trop\text{-}M}$) driven by tropospheric $O_3$, $H_2O_{(g)}$, and boundary layer $NO_x$. (d) Regional mean $[OH]_{trop\text{-}M}$ changes over South Asia.

**Extended Data Figure 4. Contributions of boundary layer $NO_x$ to anomaly in $[OH]_{trop\text{-}M}$ during the Covid-lockdown period in 2020.** The lockdown period is 2020.3-2020.5 for Eastern United States and Western Europe, and 2020.2-2020.3 for Eastern China.

**Extended Data Figure 5. Regional contributions of individual OH precursors (various colors) to global $CH_4$ sink changes during unusual years.** (a) The rapid increase in the global $CH_4$ sink following 2007 (mean values of 2008–2009 minus 2006–2007). (b) Anomaly in the global $CH_4$ sink during the El Niño event starting in 2015 (mean values of 2015.5-2016.4 minus 2014.5-2015.4). (c–d) Anomalies in the global $CH_4$ sink during the COVID-19 lockdown in 2020 (2020 minus 2019) and 2021 (2021 minus 2019). Error bars represent the range of $CH_4$ sink estimates from various datasets.

**Extended Data Figure 6. Contributions of $NO_x$ from the boundary layer, free troposphere, and whole troposphere to global $[OH]_{trop\text{-}M}$ and $CH_4$ sink changes during unusual years.** The unusual years include the El Niño event starting in 2015 (mean values of 2015.5-2016.4 minus 2014.5-2015.4) and the COVID-19 lockdown in 2020 (2020 minus 2019). (a) The $[OH]_{trop\text{-}M}$. (b) Chemical loss of $CH_4$.

**Extended Data Figure 7. Conceptual diagram illustrating how air pollution modulates global OH radicals and the $CH_4$ chemical sink.** Red arrows indicate positive contributions, while blue arrows show negative contributions. Grey arrows represent the interactions between climate and air quality measures, global warming, and air pollution.